

# 2D/2D/2D heterojunction of $\text{Ti}_3\text{C}_2$ MXene/ $\text{MoS}_2$ nanosheets/ $\text{TiO}_2$ nanosheets with exposed (001) facets toward enhanced photocatalytic hydrogen production activity



Yujie Li, Zhaohua Yin, Guanrui Ji, Zhangqian Liang, Yanjun Xue, Yichen Guo, Jian Tian\*,  
Xinzheng Wang\*, Hongzhi Cui\*

School of Materials Science and Engineering, Shandong University of Science and Technology, Qingdao 266590, China

## ARTICLE INFO

### Keywords:

Photocatalytic  $\text{H}_2$  production  
Exposed active facet  
 $\text{Ti}_3\text{C}_2$  MXene  
 $\text{MoS}_2$  nanosheets  
 $\text{TiO}_2$  nanosheets

## ABSTRACT

Exposing the highly active facets and hybridizing the photocatalyst with appropriate cocatalysts with right placement have been regarded as a powerful approach to high performance photocatalysts. Herein,  $\text{TiO}_2$  nanosheets (NSs) are *in situ* grown on highly conductive  $\text{Ti}_3\text{C}_2$  MXene and then  $\text{MoS}_2$  NSs are deposited on the (101) facets of  $\text{TiO}_2$  NSs with mainly exposed high-active (001) facets through a two-step hydrothermal method. And a unique 2D-2D-2D structure of  $\text{Ti}_3\text{C}_2@\text{TiO}_2@\text{MoS}_2$  composite is achieved. With an optimized  $\text{MoS}_2$  loading amounts (15 wt%), the  $\text{Ti}_3\text{C}_2@\text{TiO}_2@\text{MoS}_2$  composite shows a remarkable enhancement in the photocatalytic  $\text{H}_2$  evolution reaction compared with  $\text{Ti}_3\text{C}_2@\text{TiO}_2$  composite and  $\text{TiO}_2$  NS. It also shows good stability under the reaction condition. This arises from: (i) the *in situ* growth of  $\text{TiO}_2$  NSs construct strong interfacial contact with excellent electronic conductivity of  $\text{Ti}_3\text{C}_2$ , which facilitates the separation of carriers; (ii) the coexposed (101) and (001) facets can form a surface heterojunction within single  $\text{TiO}_2$  NS, which is beneficial for the transfer and separation of charge carriers; and (iii) the  $\text{MoS}_2$  NSs are deposited on the electrons-rich (101) facets of  $\text{TiO}_2$  NSs, which not only effectively reduces the charge carriers recombination rate by capturing photoelectrons, but also makes  $\text{TiO}_2$  NSs expose more highly active (001) facets to afford high-efficiency photogeneration of electron-hole pairs.

## 1. Introduction

To solve the ever increasing global demands for energy crisis and environmental protection, the development of clean energy has attracted great attention recently [1,2]. Hydrogen evolution *via* photocatalytic water splitting is a promising approach to alleviating the energy and environmental crisis [3–5].  $\text{TiO}_2$  is one of the most important semiconductor-based photocatalysts and has been widely studied for photocatalytic  $\text{H}_2$  production [6,7]. However, the application of  $\text{TiO}_2$  is restricted due to the rapid recombination of photo-generated electron-hole pairs, so massive scientific endeavors (for instance, surface modification, cocatalyst loading, impurity doping and heterojunction construction) have been devoted to promote photo-induced electrons and holes separation over the  $\text{TiO}_2$ -based photocatalysts [8,9]. Since Yang et al. found that the 47% exposed active (001) facets of  $\text{TiO}_2$  nanosheets (NSs) showed the highest photocatalytic activity [10], morphology engineering of  $\text{TiO}_2$  that can attain exposed high-active crystal facets is a promising approach to enhance the photocatalytic activity [11].  $\text{TiO}_2$

has three different exposed facets: (001), (100) and (101). The order of the average surface energies of crystal facets follows  $0.90 \text{ J/m}^2$  for (001)  $> 0.53 \text{ J/m}^2$  for (100)  $> 0.44 \text{ J/m}^2$  for (101) [12]. Besides,  $\text{TiO}_2$  NSs with exposed (101) and (001) facets can form a surface heterojunction, which is beneficial for the transfer of photogenerated electrons and holes to (101) and (001) facets [13].

Herein, we propose a new design of  $\text{TiO}_2$ -based photocatalyst with dual co-catalysts, in which both two-dimensional (2D)  $\text{Ti}_3\text{C}_2$  MXene and  $\text{MoS}_2$  NSs act as electron mediators and reduction cocatalysts. Recently, MXenes, a new family of 2D transition metal carbides, have been successfully synthesized by selective exfoliation of ternary carbides, nitrides, or carbonitrides with a general formula of  $\text{M}_{n+1}\text{X}_n$ , where M represents transition metals (such as Sc, Ti, Ta, Cr, Mo, etc.) and X is carbon and/or nitrogen [14–16]. The density functional theory (DFT) calculations indicate that MXenes exhibit metallic conductivity, which have been explored for catalysis, energy storage and conversion [17,18]. The experimental characterizations have also been demonstrated crucial to be the effective electrocatalysts in the hydrogen

\* Corresponding authors.

E-mail addresses: [jiantian@sdust.edu.cn](mailto:jiantian@sdust.edu.cn) (J. Tian), [xzwang@sdust.edu.cn](mailto:xzwang@sdust.edu.cn) (X. Wang), [cuihongzhi1965@163.com](mailto:cuihongzhi1965@163.com) (H. Cui).

evolution reaction (HER) [19,20], indicating that MXenes may be a good cocatalyst for photocatalytic H<sub>2</sub>. These unique electronic properties suggest the potential of MXene as a promoter for the transfer and accumulation of charge carrier, which can cause a negative shift and alignment of the Fermi level and improve the photocatalytic water splitting [21,22]. Molybdenum disulfide (MoS<sub>2</sub>) is also a typical 2D layered transition metal sulfide with a structure composed of three stacked atom layers, composed of Mo atoms sandwiched between two layers of hexagonally close-packed sulfur atoms (S-Mo-S) [23]. MoS<sub>2</sub> can be used as a promising cost-effective cocatalysts and shows superior photocatalytic H<sub>2</sub> production activity, due that the unsaturated S atoms on the exposed edges of MoS<sub>2</sub> act as active sites and have a strong affinity to H<sup>+</sup> in solution [24]. More importantly, the unique 2D structure of MXenes and MoS<sub>2</sub> with rich surface groups favors the construction of 2D-2D-2D heterojunction based on MXenes, MoS<sub>2</sub> and 2D semiconductors, establishing strong interface contact between cocatalyst and photocatalyst. Such 2D-2D-2D heterojunction with intimate contact can greatly improve the transfer and separation of photo-induced charge carriers across the heterojunction interface due to intense physical and electronic coupling effects [25].

In this paper, the design motif is the grafting of *in situ* growth of TiO<sub>2</sub> NSs on the Ti<sub>3</sub>C<sub>2</sub> MXene and MoS<sub>2</sub> NSs on the (101) facets of TiO<sub>2</sub> NSs with mainly exposed high-active (001) facets via a two-step hydrothermal method. In this design, electrons and holes are photo-generated on the (001) surfaces of TiO<sub>2</sub>, the most active surface for photocatalysis. Besides, the high electronic conductivity of Ti<sub>3</sub>C<sub>2</sub> MXene acts as a source of titanium and a pathway transferring photo-generated electrons to enhance the separation efficiency of charges. Furthermore, the photogenerated electrons and holes can be respectively transferred onto (101) and (001) facets of TiO<sub>2</sub> due to the presence of surface heterojunction. Moreover, the deposited of MoS<sub>2</sub> NSs on the (101) facets of TiO<sub>2</sub> NSs can capture photogenerated electrons of (101) facets and act as reduction active sites. Through this design, the photogenerated charge carriers are effectively separated, and the activity of photocatalytic H<sub>2</sub> production is improved, showing the promise of dual cocatalyst strategy for photocatalysis.

## 2. Experimental procedure

### 2.1. Materials

The Ti<sub>3</sub>AlC<sub>2</sub> powder was provided by Hello Nano Technology Co., Ltd., Changchun. Hydrofluoric acid (HF, 40 wt%), hydrochloric acid (HCl), sodium tetrafluoroborate (NaBF<sub>4</sub>), sodium molybdate dihydrate (Na<sub>2</sub>MoO<sub>4</sub>·2H<sub>2</sub>O), and thiourea (CN<sub>2</sub>H<sub>4</sub>S) were purchased from Sinopharm. All chemicals used were of analytical reagent grade.

### 2.2. Preparation of Ti<sub>3</sub>C<sub>2</sub> MXene

Typically, 1 g Ti<sub>3</sub>AlC<sub>2</sub> powders were slowly added to 200 mL 40 wt % HF solution. Then the reaction mixtures were stirred for 72 h at room temperature. After that, the mixed solutions were washed with deionized water to neutral, and the powders were collected after discarding the supernatant. Finally, Ti<sub>3</sub>C<sub>2</sub> MXene was dried in vacuum oven at 50 °C for 12 h.

### 2.3. Preparation of Ti<sub>3</sub>C<sub>2</sub>@TiO<sub>2</sub> composites and TiO<sub>2</sub> nanosheets (NSs)

To synthesis of Ti<sub>3</sub>C<sub>2</sub>@TiO<sub>2</sub> composites, 100 mg Ti<sub>3</sub>C<sub>2</sub> MXene and 0.1 M NaBF<sub>4</sub> were added into 15 ml of 1.0 M HCl. After the solution had been stirred for 30 min, it was transferred into a 25 mL Teflon-lined stainless-steel autoclave, which was hydrothermally treated at 160 °C for 12 h. After naturally cooling down to room temperature, the reaction solution was collected by vacuum filtration, and the resulting Ti<sub>3</sub>C<sub>2</sub>@TiO<sub>2</sub> composites were washed with distilled water several times, and dried in vacuum oven at 60 °C for 12 h.

For comparison, pure TiO<sub>2</sub> NSs were also synthesized with Ti(OBu)<sub>4</sub> as the source of titanium. In the synthesis process, 0.5 mL Ti(OBu)<sub>4</sub> and 0.15 g CFs were slowly dropped into HCl (9 mL, 5 M) solution. After the solution was stirred for 30 min, then 0.2 mL HF was added to the mixed solution. And the solutions were transferred into Teflon-lined stainless-steel autoclaves with a total volume of 25 mL. The hydrothermal synthesis was conducted at 180 °C for 4 h in an electric oven. The obtained CF@TiO<sub>2</sub> composites were heated at 800 °C for 2 h to remove the CF templates.

### 2.4. Preparation of Ti<sub>3</sub>C<sub>2</sub>@TiO<sub>2</sub>@MoS<sub>2</sub> composites

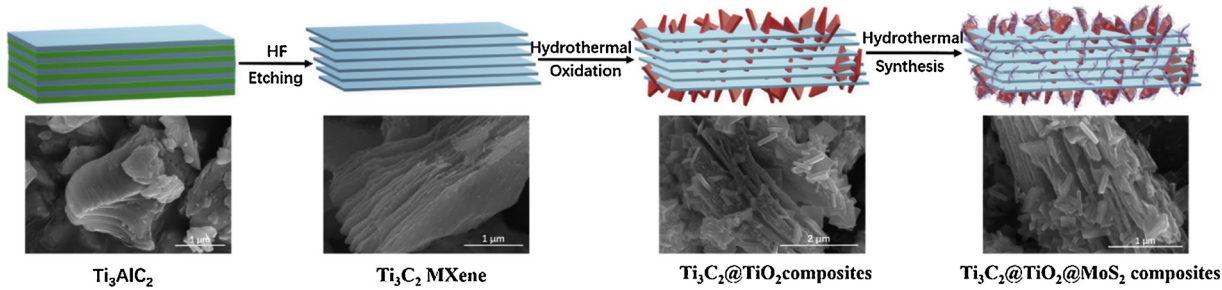
To synthesis of Ti<sub>3</sub>C<sub>2</sub>@TiO<sub>2</sub>@MoS<sub>2</sub> composites, 15 mg Na<sub>2</sub>MoO<sub>4</sub>·2H<sub>2</sub>O and 30 mg CN<sub>2</sub>H<sub>4</sub>S were dissolved in 20 mL deionized water to form a transparent solution. Then, 60 mg Ti<sub>3</sub>C<sub>2</sub>@TiO<sub>2</sub> composites was added into the above solution and stirred to form the suspension. The suspension was transferred into a 25 mL Teflon-lined stainless-steel autoclave, which was hydrothermally treated at 200 °C for 24 h. After naturally cooling down to room temperature, the reaction solution was collected by vacuum filtration, and the resulting Ti<sub>3</sub>C<sub>2</sub>@TiO<sub>2</sub>@MoS<sub>2</sub> composites (15 wt% MoS<sub>2</sub>) were washed with distilled water several times, and dried in vacuum oven at 50 °C for 12 h. Similarity, by changing the mass of Na<sub>2</sub>MoO<sub>4</sub>·2H<sub>2</sub>O (7.5 mg, 23 mg, and 30 mg) and CN<sub>2</sub>H<sub>4</sub>S (15 mg, 46 mg, 60 mg), Ti<sub>3</sub>C<sub>2</sub>@TiO<sub>2</sub>@MoS<sub>2</sub> composites with other MoS<sub>2</sub> loading amounts (10 wt%, 25 wt%, 30 wt%) were obtained, respectively.

### 2.5. Characterization

The phase constituents of the synthesized products were analyzed by X-ray diffraction (XRD, D/Max 2500PC Rigaku, Japan) with Cu K $\alpha$  ( $\lambda = 0.15406$  nm) radiation source. The nanostructure and surface characteristic of the products were observed with a high-resolution scanning electron microscope (FESEM, FEI Nova Nanosem 450, USA) with an energy-dispersive X-ray spectroscopy (EDS). High transmission electron microscopy (HRTEM) was carried out with a JEOL JEM 2100 F field emission transmission electron microscope. The chemical states of the composite were tested using X-ray photoelectron spectrometry measurements (XPS, Thermo ESCALAB 250XI, USA). The UV-vis diffuse reflectance spectra (DRS) of the samples were tested on a UV-vis spectrophotometer (Hitachi UV-3101) with an integrating sphere attachment within 200–800 nm range and with BaSO<sub>4</sub> as the reflectance standard. The surface area was measured using the Brunauer Emmett Teller (BET) method as-examined on a Micromeritics ASAP2020 nitrogen adsorption–desorption apparatus. The photoluminescence (PL) spectra were acquired at room temperature with a FLS920 fluorescence spectrometer under the ultraviolet excitation of 325 nm.

### 2.6. Photocatalytic and photoelectrochemical activity test

The photocatalytic reaction was implemented in a Pyrex glass vessel, with a top quartz window suitable for vertical illumination, connected to a gastight circulation system. A 300 W Xe arc lamp (CELHXF300, Beijing China Education Au-light Co., Ltd.) with an AM-1.5 filter was used as the light source. The experiments were performed in aqueous acetone with dissolved sacrificial reagent (TEOA), and suspended with 10 mg of catalysts powder following ultrasonic dispersion for 10 min. Then the reaction solution was evacuated several times to remove air and the reaction temperature of reactant solution was maintained at 25 °C. The amount of the generated hydrogen was analyzed by a gas chromatograph (Techcomp GC-7920) equipped with a thermal conductivity detector (TCD). The apparent quantum efficiency (AQE) was measured under the same light source. The focused intensity on the flask was *ca.* 513 mW/cm<sup>2</sup>. The AQE was calculated according to the following equations:



**Scheme 1.** Schematic illustration of the preparation of  $\text{Ti}_3\text{C}_2\text{@}\text{TiO}_2\text{@}\text{MoS}_2$  composites.

$$\begin{aligned}
 \text{AQE} &= \frac{\text{number of reacted electrons}}{\text{number of incident photons}} \times 100\% \\
 &= \frac{2 \times \text{number of evolved hydrogen molecules}}{\text{number of incident photons}} \times 100\%
 \end{aligned} \quad (1)$$

Transient photocurrent responses (PEC) and electrochemical impedance spectroscopy (EIS) curves were measured under a 300 W Xe arc lamp with an AM-1.5 filter with light on-off switches of 100 s in a three-electrode electrochemical cell in the 0.5 M  $\text{Na}_2\text{SO}_4$  electrolyte, in which Pt wire and Ag/AgCl electrode were used as the counter and reference electrodes, respectively. 5 mg as-synthesized samples were mixed with 0.5 mL ethanol and terpineol. After sonicated for 5 min, the mixture was dropped onto fluoride-tin oxide (FTO) conductor glass and dried at 50 °C for 6 h to form a working electrode.

### 3. Results and discussion

**Scheme 1** describes the synthesis strategy of the hybrid structures of the  $\text{Ti}_3\text{C}_2\text{@}\text{TiO}_2\text{@}\text{MoS}_2$  composites. Firstly, The  $\text{Ti}_3\text{AlC}_2$  ceramics (MAX phase) are firstly etched by HF to remove the Al layers [26]. Secondly, the *in-situ* growth of  $\text{TiO}_2$  NSs with preferentially exposed (001) facets from the layered  $\text{Ti}_3\text{C}_2$  MXene are got through the hydrothermal oxidation of  $\text{Ti}_3\text{C}_2$  in the assistance of HCl and  $\text{NaBF}_4$ . The formation of  $\text{TiO}_2$  NSs with abundant high-activity (001) surfaces can improve the photocatalytic activity. Subsequently, the obtained  $\text{Ti}_3\text{C}_2\text{@}\text{TiO}_2$  composites are immersed in a clear solution with  $\text{Na}_2\text{MoO}_4\text{:}2\text{H}_2\text{O}$  and  $\text{CN}_2\text{H}_4\text{S}$  at 200 °C for 24 h in order to introduce  $\text{MoS}_2$  cocatalyst. Ultimately,  $\text{MoS}_2$  NSs are deposited onto (101) facets of  $\text{TiO}_2$  NSs to form the ternary  $\text{Ti}_3\text{C}_2\text{@}\text{TiO}_2\text{@}\text{MoS}_2$  composites.

The etching of  $\text{Ti}_3\text{AlC}_2$  and the formation of  $\text{Ti}_3\text{C}_2$  and  $\text{Ti}_3\text{C}_2\text{@}\text{TiO}_2$  composites were clearly revealed by XRD analysis. The MAX phase exhibits intense peaks, which can be assigned to  $\text{Ti}_3\text{AlC}_2$  according to previous reports [26,27]. After  $\text{Ti}_3\text{AlC}_2$  was etched by HF, as expected, the most intense (104) diffraction peak in  $\text{Ti}_3\text{AlC}_2$  pattern located at 39° completely disappeared (Fig. 1a). The (002) at 9.58° and (004) at

19.17° of  $\text{Ti}_3\text{AlC}_2$  were broadened and shifted toward lower angle side, indicating the transformation from  $\text{Ti}_3\text{AlC}_2$  to  $\text{Ti}_3\text{C}_2$  MXene [28]. The hydrothermal oxidation of  $\text{Ti}_3\text{C}_2$  caused the growth of  $\text{TiO}_2$  NSs across the layered  $\text{Ti}_3\text{C}_2$  sheets, evidenced by the SEM image in **Scheme 1** and the emergence of XRD reflections from anatase  $\text{TiO}_2$  (Fig. 1a, JCPDS No. 21-1272). For  $\text{Ti}_3\text{C}_2\text{@}\text{TiO}_2\text{@}\text{MoS}_2$  composites with different  $\text{MoS}_2$  loading amounts (Fig. 1b), all the diffraction peaks could be well indexed to the  $\text{Ti}_3\text{C}_2$  or anatase  $\text{TiO}_2$ . No signals assignable to  $\text{MoS}_2$  are detectable. This can be explained by the fact that  $\text{MoS}_2$  is ultra-thin and is high dispersed on the  $\text{Ti}_3\text{C}_2\text{@}\text{TiO}_2\text{@}\text{MoS}_2$  composites.

The morphology of  $\text{Ti}_3\text{C}_2$  MXene,  $\text{Ti}_3\text{C}_2\text{@}\text{TiO}_2$  composites, and  $\text{Ti}_3\text{C}_2\text{@}\text{TiO}_2\text{@}\text{MoS}_2$  composites with different  $\text{MoS}_2$  loading amounts were characterized by scanning electron microscopy (SEM) (Figs. 2, S1 and S2). As shown in Fig. 2a, as the Al atoms between layers are removed after HF etching, the formed loose accordion-shape layered structure reveals the typical MXene morphology. After hydrothermal oxidation of  $\text{Ti}_3\text{C}_2$  MXene, a lot of nanosheets are sidelinked inserted across the stack of  $\text{Ti}_3\text{C}_2$  MXene to form 2D-2D  $\text{Ti}_3\text{C}_2\text{@}\text{TiO}_2$  composites (Fig. 2b). These nanosheets are anatase  $\text{TiO}_2$  with exposed (001) surfaces which are *in situ* grown due to the introduction of HCl and  $\text{NaBF}_4$  during the delamination of  $\text{Ti}_3\text{C}_2$ . Under the acidic hydrothermal conditions, the layered  $\text{Ti}_3\text{C}_2$  provides Ti sources for the growth of  $\text{TiO}_2$  [29]. Assisted by the directing reagent  $\text{NaBF}_4$ , the formation of high-energy (001) facets is enhanced during the sequential crystal growth, because of the lower energy of (101) planes adsorbing  $\text{F}^-$  [25,30–32]. The  $\text{TiO}_2$  NSs with the most active (001) facets can be homogeneously distributed around the layered  $\text{Ti}_3\text{C}_2$  to provide improved accessibility to light and reactants. More importantly, the 2D  $\text{Ti}_3\text{C}_2$  sheets traverse  $\text{TiO}_2$  nanocrystals at the most active (001) facets, as shown in Fig. 2b. The intimate contact between these two phases might facilitate the separation of charge carriers photogenerated on the (001) surfaces, thereby improving the photocatalytic activity.

For  $\text{Ti}_3\text{C}_2\text{@}\text{TiO}_2\text{@}\text{MoS}_2$  composites (15 wt%  $\text{MoS}_2$ ), it should be noted that most of  $\text{MoS}_2$  NSs with a very thin layer can be found on the (101) facets of  $\text{TiO}_2$  NSs in  $\text{Ti}_3\text{C}_2\text{@}\text{TiO}_2$  composites (Fig. 2c), while a

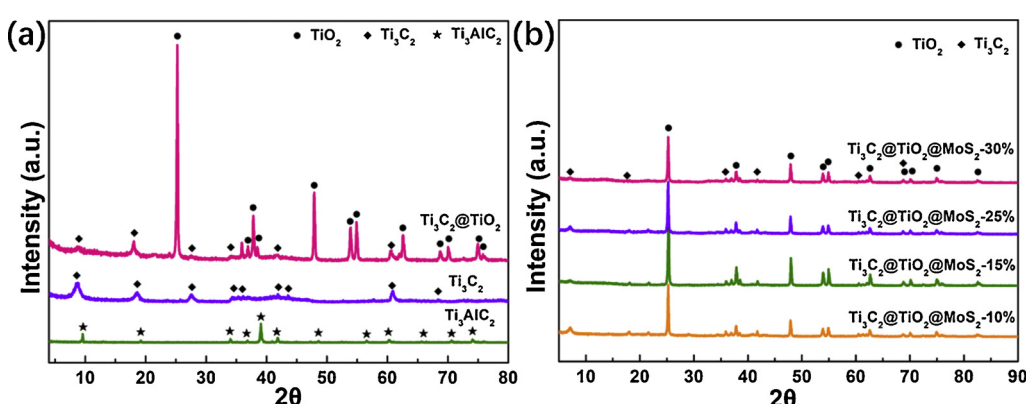


**Fig. 1.** XRD patterns of (a)  $\text{Ti}_3\text{AlC}_2$ ,  $\text{Ti}_3\text{C}_2$  MXene,  $\text{Ti}_3\text{C}_2\text{@}\text{TiO}_2$  composites and (b)  $\text{Ti}_3\text{C}_2\text{@}\text{TiO}_2\text{@}\text{MoS}_2$  composites with different  $\text{MoS}_2$  loading amounts (10 wt%, 15 wt%, 20 wt%, 25 wt%, 30 wt%).

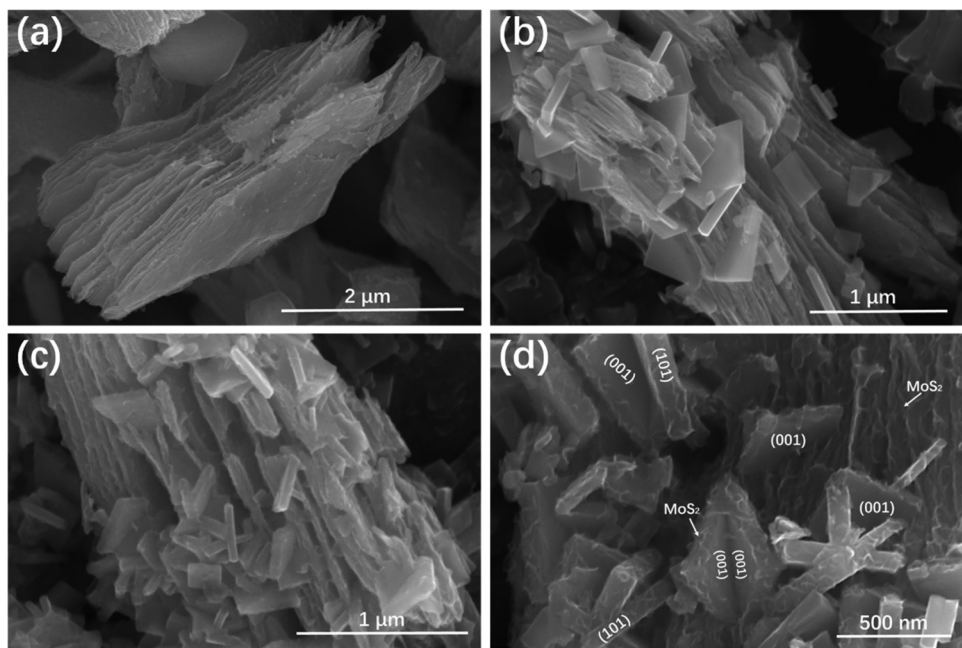


Fig. 2. SEM images of (a) Ti<sub>3</sub>C<sub>2</sub> MXene, (b) Ti<sub>3</sub>C<sub>2</sub>@TiO<sub>2</sub> composites, and (c, d) Ti<sub>3</sub>C<sub>2</sub>@TiO<sub>2</sub>@MoS<sub>2</sub> composites (15 wt% MoS<sub>2</sub>).

few of MoS<sub>2</sub> NSs are observed on the (001) facets. This phenomenon is also confirmed by a magnified FE-SEM image of Ti<sub>3</sub>C<sub>2</sub>@TiO<sub>2</sub> composites (Fig. 2d), which can keep the maximum exposure of (001) facets of TiO<sub>2</sub> NSs with higher surface energy. Furthermore, Ti<sub>3</sub>C<sub>2</sub>@TiO<sub>2</sub>@MoS<sub>2</sub> composites with other different MoS<sub>2</sub> loading amounts (10 wt%, 25 wt %, 30 wt%) are also obtained, the corresponding SEM images are shown in Fig. S1. The SEM images of pure TiO<sub>2</sub> NSs and TiO<sub>2</sub>@MoS<sub>2</sub> composites (15 wt%) are shown in Fig. S2. As shown in Fig. S2a, TiO<sub>2</sub> NS still keep a sheet shaped structure with co-exposed (001) and (101) facets. For TiO<sub>2</sub>@MoS<sub>2</sub> composites (15 wt% MoS<sub>2</sub>), most of MoS<sub>2</sub> NSs are assembled on the (101) facets of TiO<sub>2</sub> NSs (Fig. S2b). Moreover, The EDS mapping images and point scan (Figs. S3, S4 and Table S1) shows that Ti, C, O, Mo and S elements can be observed in the Ti<sub>3</sub>C<sub>2</sub>@TiO<sub>2</sub>@MoS<sub>2</sub> composites, and no other impurities are observed.

Taking advantage of transmission electron microscope (TEM) can give an insight into the heterojunctions between the Ti<sub>3</sub>C<sub>2</sub>, TiO<sub>2</sub> and MoS<sub>2</sub>. Fig. 3 shows the TEM images of Ti<sub>3</sub>C<sub>2</sub>@TiO<sub>2</sub>@MoS<sub>2</sub> composites. Under the low magnification (Fig. 3a and b), a 2D transparent layered structure can be observed which possess the unique texture of the delaminated MXene sample and decorated with some TiO<sub>2</sub> NSs and MoS<sub>2</sub> NSs. The clearly-observed lattice fringes of the Ti<sub>3</sub>C<sub>2</sub>, TiO<sub>2</sub> and MoS<sub>2</sub> (Fig. 3c) suggested successful preparation of the Ti<sub>3</sub>C<sub>2</sub>@TiO<sub>2</sub>@MoS<sub>2</sub> composite. In detail, the lattices with d spaces of 0.98, 0.62 and 0.35 nm

are attributed to the (002) planes of Ti<sub>3</sub>C<sub>2</sub> MXene, the (002) planes of MoS<sub>2</sub>, and the (101) planes of TiO<sub>2</sub>, respectively [31–33]. Interestingly, thin MoS<sub>2</sub> NSs are intimately deposited on the (101) facets of TiO<sub>2</sub> NSs with few layers. All these results of electron microscopy strongly suggest the uniform and intimate coupling between Ti<sub>3</sub>C<sub>2</sub>, TiO<sub>2</sub> and MoS<sub>2</sub> NSs, namely, the successful construction of 2D-2D-2D heterojunction of Ti<sub>3</sub>C<sub>2</sub>@TiO<sub>2</sub>@MoS<sub>2</sub> composites. Such heterojunction is featured with large contact area between cocatalyst and photocatalyst, effectively facilitating the interfacial charge transfer during the photocatalytic reactions [34].

Ti<sub>3</sub>C<sub>2</sub>@TiO<sub>2</sub>@MoS<sub>2</sub> composites is investigated to further confirm the chemical composition and states of elements, the results are shown in Fig. 4. From the survey scan of the Ti<sub>3</sub>C<sub>2</sub>@TiO<sub>2</sub>@MoS<sub>2</sub> composites (Fig. 4a), the concomitant of Ti, C, O, Mo and S elements were detected, in concert with EDS mapping, whereas impurity F element can also be found because of the residue F ions from the HF solution. The peak located at 685 eV can be attributed to the F<sup>−</sup> ions physically adsorbed on the surface of Ti<sub>3</sub>C<sub>2</sub>@TiO<sub>2</sub>@MoS<sub>2</sub> composites (Fig. S5). The Ti 2p XPS spectra of Ti<sub>3</sub>C<sub>2</sub>@TiO<sub>2</sub>@MoS<sub>2</sub> composites can be deconvoluted into two doublet peaks (Fig. 4b). The two peaks at binding energies of 459.3 eV (Ti 2p<sub>3/2</sub>) and 465.1 eV (Ti 2p<sub>1/2</sub>) are attributed to the lattice Ti–O bond in TiO<sub>2</sub> [35], while the other two peaks at binding energies of 455.5 eV (Ti 2p<sub>3/2</sub>) and 461.6 eV (Ti 2p<sub>1/2</sub>) correspond to the lattice

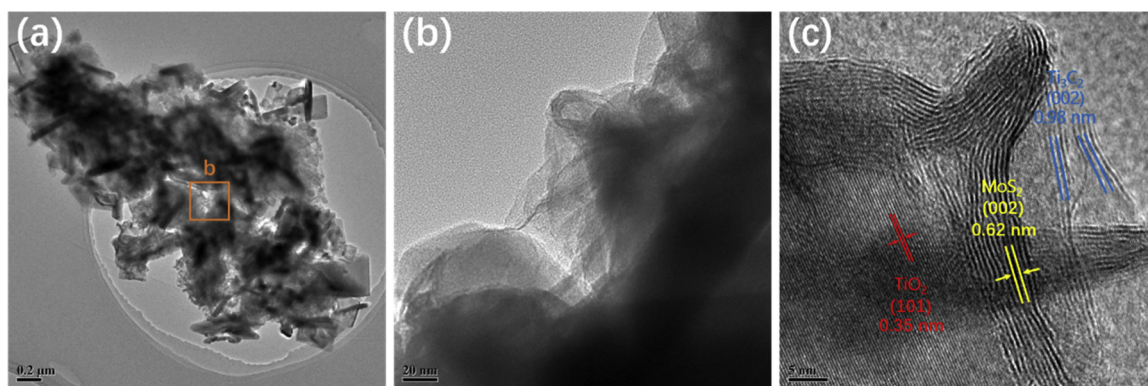


Fig. 3. TEM images of Ti<sub>3</sub>C<sub>2</sub>@TiO<sub>2</sub>@MoS<sub>2</sub> composites (15 wt% MoS<sub>2</sub>).

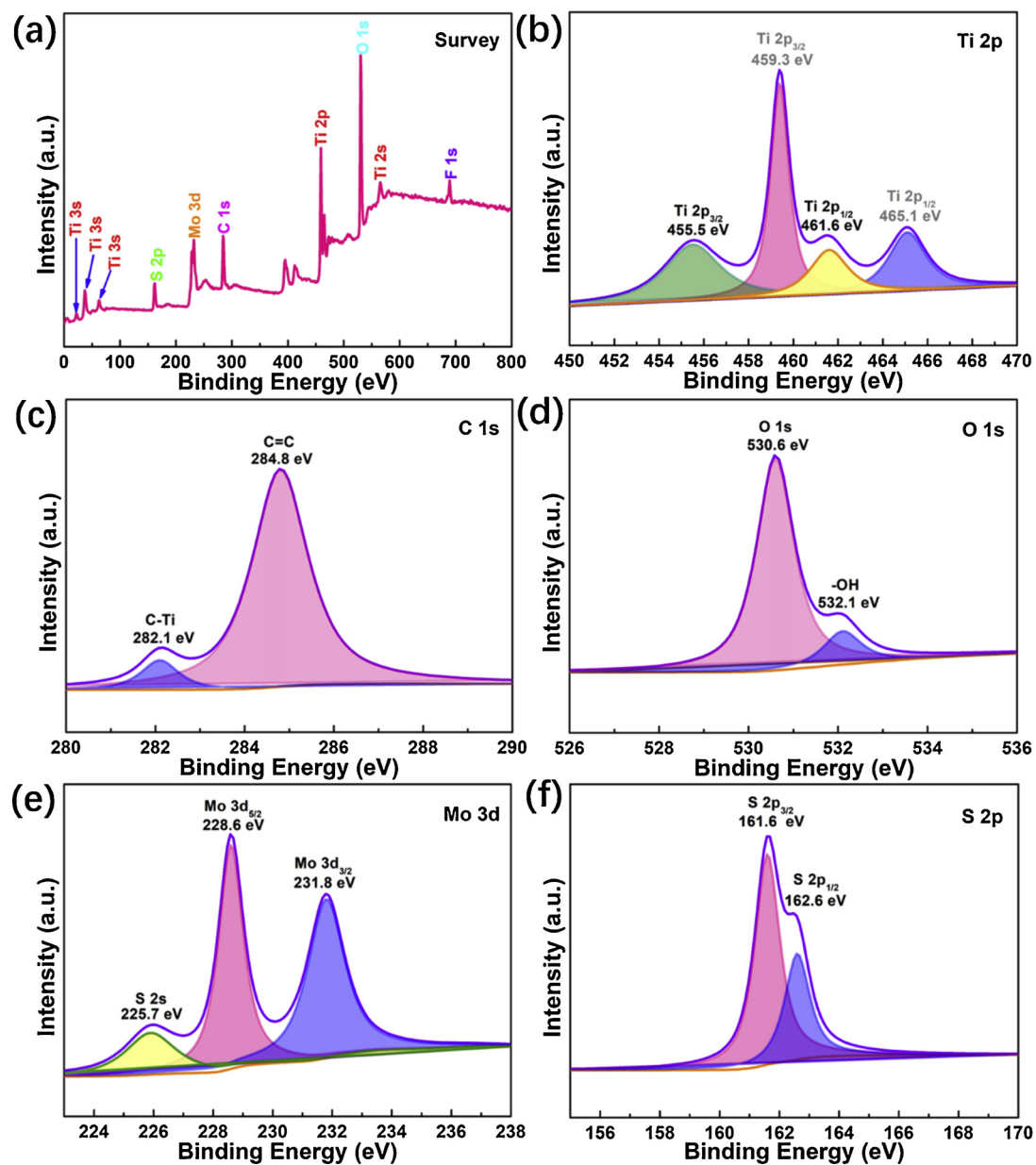


Fig. 4. XPS spectra of (a) fully scanned spectra, (b) Ti 2p, (c) C 1s, (d) O 1s, (e) Mo 3d and (f) S 2p in  $\text{Ti}_3\text{C}_2@\text{TiO}_2@\text{MoS}_2$  composites (15 wt%  $\text{MoS}_2$ ).

Ti–C bond in  $\text{Ti}_3\text{C}_2$  [25]. Furthermore, the C 1s XPS spectrum of  $\text{Ti}_3\text{C}_2@\text{TiO}_2@\text{MoS}_2$  composites exhibits two obvious peaks at 284.8 and 282.1 eV, designated to  $\text{sp}^2$  carbon ( $\text{C}=\text{C}$ ) and C–Ti, respectively. Those are attributed to the adventitious elemental carbon and  $\text{Ti}_3\text{C}_2$  (Fig. 4c) [31]. With respect to the O 1s XPS spectra, two peaks at 530.6 and 532.1 eV have been deconvoluted (Fig. 4d), which are ascribed to Ti–O–Ti (lattice O) and surface hydroxyl groups [36], respectively. The Mo 3d XPS spectra of  $\text{Ti}_3\text{C}_2@\text{TiO}_2@\text{MoS}_2$  composites (Fig. 4e) can be deconvoluted into two peaks at 231.8 and 228.6 eV, attributed to the  $\text{Mo 3d}_{3/2}$  and  $\text{Mo 3d}_{5/2}$  of  $\text{Mo}^{4+}$  in  $\text{MoS}_2$ , respectively [32]. The S 2p high-resolution spectra (Fig. 4f) of the  $\text{Ti}_3\text{C}_2@\text{TiO}_2@\text{MoS}_2$  composites displays two main peaks at 162.6 and 161.6 eV, corresponding to the  $\text{S 2p}_{1/2}$  and  $\text{S 2p}_{3/2}$  doublet of  $\text{S}^{2-}$  in  $\text{MoS}_2$  [37].

The nitrogen adsorption–desorption isotherms and the corresponding pore size distribution curves (inset) of the samples are shown in Fig. 5 and S6, and the specific surface areas are listed in Table S2. The pore size distribution curve (Fig. 5a–d inset) of the  $\text{Ti}_3\text{C}_2@\text{TiO}_2@\text{MoS}_2$  composites reveals that the pore size is mainly mesopore, and the average pore size diameter is about 3 nm, which are similar to  $\text{Ti}_3\text{C}_2$

and  $\text{Ti}_3\text{C}_2@\text{TiO}_2$  composites (Fig. S6a and b), while the average pore size diameter of  $\text{MoS}_2$  NSs is about 5.5 nm (Fig. S6c). As it has been reported in the previous works, all samples have the isotherms of type IV with a typical H3 hysteresis loop, suggesting the slit-like mesoporous character of the samples (Figs. 5 and S6) [26,38–40]. The BET surface area of  $\text{Ti}_3\text{C}_2$ ,  $\text{MoS}_2$ ,  $\text{Ti}_3\text{C}_2@\text{TiO}_2$ ,  $\text{Ti}_3\text{C}_2@\text{TiO}_2@\text{MoS}_2$ –10%,  $\text{Ti}_3\text{C}_2@\text{TiO}_2@\text{MoS}_2$ –15%,  $\text{Ti}_3\text{C}_2@\text{TiO}_2@\text{MoS}_2$ –25%, and  $\text{Ti}_3\text{C}_2@\text{TiO}_2@\text{MoS}_2$ –30% are 7.097, 6.302, 13.951, 18.894, 20.065, 16.374 and 15.156  $\text{m}^2 \text{g}^{-1}$ , respectively (Table S2). The  $\text{Ti}_3\text{C}_2@\text{TiO}_2@\text{MoS}_2$ –15% exhibits a higher surface area than others, which is beneficial for the adsorption and migration of reactant and product molecules.

The photocatalytic performance is greatly determined by the optical absorption property. The solar light harvesting of the samples were investigated through UV–vis diffuse reflectance spectra (UV–vis DRS), as shown in Fig. 6. The  $\text{Ti}_3\text{C}_2$  MXene and  $\text{MoS}_2$  NSs show an enhanced visible absorption due to the black color nature [41]. Pure  $\text{TiO}_2$  NSs possess an obvious absorption in the UV region, and no optical absorption in the visible region, which is consistent with anatase  $\text{TiO}_2$  [42]. After coupled with partially oxidative  $\text{Ti}_3\text{C}_2$  and  $\text{MoS}_2$ , the optical

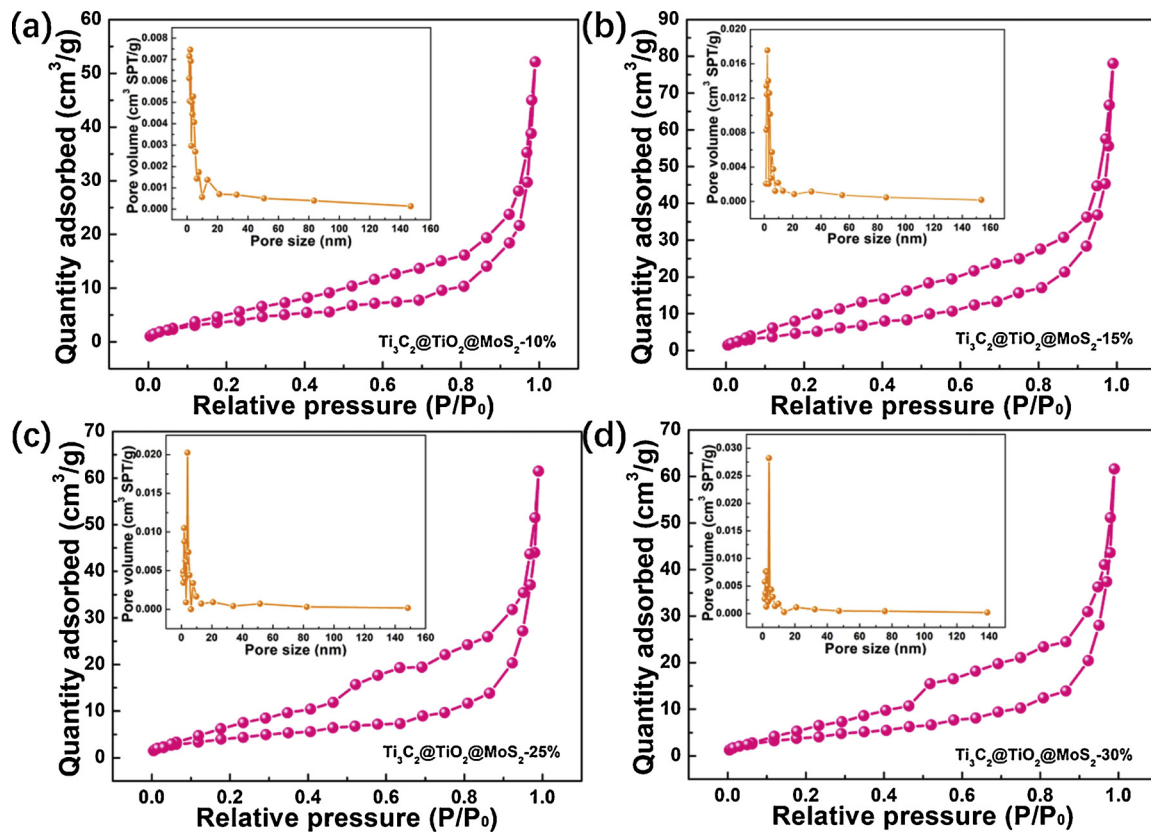


Fig. 5. N<sub>2</sub> adsorption–desorption isotherms and the corresponding pore size distribution curves (inset) of Ti<sub>3</sub>C<sub>2</sub>@TiO<sub>2</sub>@MoS<sub>2</sub> composites with different MoS<sub>2</sub> loading amounts: (a) 10 wt%, (b) 15 wt%, (c) 25 wt%, and (d) 30 wt%.

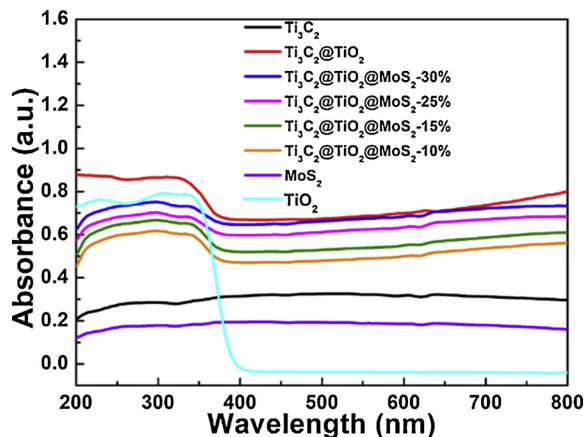


Fig. 6. UV-vis absorption spectra of Ti<sub>3</sub>C<sub>2</sub> MXene, Ti<sub>3</sub>C<sub>2</sub>@TiO<sub>2</sub> composites, TiO<sub>2</sub> NSs, Ti<sub>3</sub>C<sub>2</sub>@TiO<sub>2</sub>@MoS<sub>2</sub> composites (10 wt%, 15 wt%, 25 wt% and 30 wt% MoS<sub>2</sub>) and MoS<sub>2</sub> NSs.

absorption of Ti<sub>3</sub>C<sub>2</sub>@TiO<sub>2</sub>@MoS<sub>2</sub> composites is significantly enhanced over the UV and visible spectrum, indicating the efficiency for harvesting photons of the heterostructured sample is greatly promoted. With increasing the MoS<sub>2</sub> content, gradually increased absorption intensity can be found in the wide visible range of 420–800 nm. Such absorption is attributed to the UV/visible absorption of MoS<sub>2</sub>, which is also reflected by the dark color of the Ti<sub>3</sub>C<sub>2</sub>@TiO<sub>2</sub>@MoS<sub>2</sub> composites (Fig. S7). And the band gap energy (E<sub>g</sub>) of TiO<sub>2</sub> is calculated by the plot of transformed Kubelka-Munk function (F(R)hv)<sup>n</sup> versus the energy of exciting light (hv). Then the estimated E<sub>g</sub> of TiO<sub>2</sub> and Ti<sub>3</sub>C<sub>2</sub>@TiO<sub>2</sub>@MoS<sub>2</sub> is 3.15 and 2.70 eV (Fig. S8), respectively.

The photocatalytic activity for H<sub>2</sub> evolution was evaluated under

simulated sunlight irradiation with 300 W Xe arc lamp. Fig. 7 presents a comparison of the photocatalytic H<sub>2</sub> production activities of Ti<sub>3</sub>C<sub>2</sub> MXene, Ti<sub>3</sub>C<sub>2</sub>@TiO<sub>2</sub> composites, Ti<sub>3</sub>C<sub>2</sub>@TiO<sub>2</sub>@MoS<sub>2</sub> composites (10 wt%, 15 wt%, 25 wt% and 30 wt% MoS<sub>2</sub>) and TiO<sub>2</sub> NSs in aqueous acetone solution with TEOA. Here, acetone is a scavenger and TEOA is a sacrificial agent to quench the photo-generated holes. As shown in Fig. 7b, pure TiO<sub>2</sub> NSs are photocatalytically active but the H<sub>2</sub> evolution rates as low as 73.758 μmol h<sup>-1</sup> g<sup>-1</sup>, because of the rapid recombination of electrons and holes [43]. And there is no H<sub>2</sub> detected on Ti<sub>3</sub>C<sub>2</sub> MXene due to the metallic properties Ti<sub>3</sub>C<sub>2</sub>, consistent with the literature [44]. Nevertheless, the H<sub>2</sub> evolution rates of Ti<sub>3</sub>C<sub>2</sub>@TiO<sub>2</sub> composites is 898.128 μmol h<sup>-1</sup> g<sup>-1</sup>. As the Ti<sub>3</sub>C<sub>2</sub> presents metallic properties, the contribution to the H<sub>2</sub> production can be ascribed mainly to the high-activity (001) facets of TiO<sub>2</sub> in the Ti<sub>3</sub>C<sub>2</sub>@TiO<sub>2</sub> composites. The metallic Ti<sub>3</sub>C<sub>2</sub> in the Ti<sub>3</sub>C<sub>2</sub>@TiO<sub>2</sub> composites can attract the photo-induced electron, leave the hole behind, and promote the H<sub>2</sub> production from water. For the Ti<sub>3</sub>C<sub>2</sub>@TiO<sub>2</sub>@MoS<sub>2</sub> composites with different MoS<sub>2</sub> loading amount, the yield of H<sub>2</sub> evolution is nearly linear increase with the irradiation time prolong (Fig. 7a). An optimum H<sub>2</sub> evolution rate of 6425.297 μmol h<sup>-1</sup> g<sup>-1</sup> is obtained on Ti<sub>3</sub>C<sub>2</sub>@TiO<sub>2</sub>@MoS<sub>2</sub> composites (15 wt% MoS<sub>2</sub>) (Fig. 7b), which is much higher than other samples. Such performance enhancement can be attributed to the formation of 2D-2D-2D heterojunction of Ti<sub>3</sub>C<sub>2</sub>@TiO<sub>2</sub>@MoS<sub>2</sub> composites with the following advantages: (1) Photo-induced electrons from the conduction band (CB) of TiO<sub>2</sub> can effectively transfer across the interface of the hybrids and accumulate on the surface of Ti<sub>3</sub>C<sub>2</sub>, due to the large interface contact area and the quite short charge transport distance of the *in situ* growth of TiO<sub>2</sub> NSs on Ti<sub>3</sub>C<sub>2</sub> allowing for the interface with minimized defects [45]. (2) The introduction of Ti<sub>3</sub>C<sub>2</sub> and MoS<sub>2</sub> increases the specific surface area and enhances the water adsorption capability of the photocatalytic system. (3) Most of MoS<sub>2</sub> NSs are deposited onto electrons-rich (101) facets of

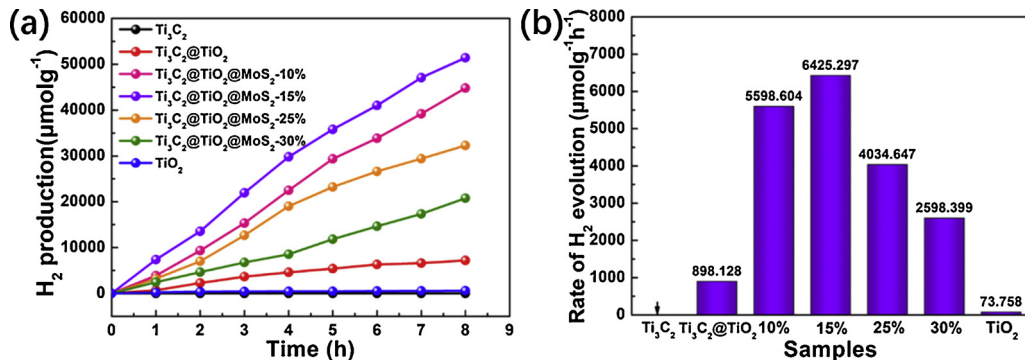


Fig. 7. (a) Photocatalytic H<sub>2</sub> production and (b) rate of photocatalytic H<sub>2</sub> production of different catalysts in aqueous acetone solution with TEOA within 8 h.

TiO<sub>2</sub> NSs with exposed (001) facets. MoS<sub>2</sub> NSs can capture photo-generated electrons of (101) facets and act as reduction active sites. The mainly high-active exposed (001) facets of TiO<sub>2</sub> NSs facilitate the activation of water molecules and the photocatalytic reduction [46]. Control experiments (Fig. S9) indicate that no appreciable H<sub>2</sub> production is detected in the absence of either irradiation or photocatalyst, suggesting that H<sub>2</sub> is produced by a photocatalytic reaction of the photocatalyst. In addition, as shown in Fig. 7b, the photocatalytic activities of the samples increase non-linearly with increasing MoS<sub>2</sub> loading (from 10 to 15 wt% MoS<sub>2</sub>), because of the relatively lower solar energy input *via* increasing catalyst amount. However, further increasing the content of MoS<sub>2</sub> (from 15 wt% to 30 wt% MoS<sub>2</sub>) leads to a gradual decrease of the photocatalytic activity. Because excess black MoS<sub>2</sub> NSs absorb photons in the photocatalytic system, probably decreasing the intensity of light through the deeper reaction solution and shielding the light from reaching the TiO<sub>2</sub> surface, which could be called a “shielding effect” [47]. The above results demonstrate clearly the significant role of Ti<sub>3</sub>C<sub>2</sub> and MoS<sub>2</sub> as effective cocatalysts in improving the photocatalytic activity of Ti<sub>3</sub>C<sub>2</sub>@TiO<sub>2</sub>@MoS<sub>2</sub> composites for H<sub>2</sub> production. We further evaluated the apparent quantum yields (AQE) of the samples under 300 W Xe arc lamp with CUT420 optical filter. As shown in Table S3, AQE values over the samples: 4.61% (Ti<sub>3</sub>C<sub>2</sub>@TiO<sub>2</sub>@MoS<sub>2</sub>-15 wt%) > 4.01% (Ti<sub>3</sub>C<sub>2</sub>@TiO<sub>2</sub>@MoS<sub>2</sub>-10 wt%) > 2.89% (Ti<sub>3</sub>C<sub>2</sub>@TiO<sub>2</sub>@MoS<sub>2</sub>-25 wt%) > 1.86% (Ti<sub>3</sub>C<sub>2</sub>@TiO<sub>2</sub>@MoS<sub>2</sub>-30 wt%) > 0.644% (Ti<sub>3</sub>C<sub>2</sub>@TiO<sub>2</sub>) > 0.0529% (TiO<sub>2</sub> NSs), which is consistent with their photocatalytic H<sub>2</sub> production. Stability and recyclability of the Ti<sub>3</sub>C<sub>2</sub>@TiO<sub>2</sub>@MoS<sub>2</sub> composites (15 wt% MoS<sub>2</sub>) were estimated by repeating intermittent H<sub>2</sub> evolution under solar light (Fig. S10). After 3 cycles, the photocatalytic H<sub>2</sub> production rate of the Ti<sub>3</sub>C<sub>2</sub>@TiO<sub>2</sub>@MoS<sub>2</sub> composites did not show pronounced change, indicating its excellent photostability. Besides, XRD pattern and SEM image of Ti<sub>3</sub>C<sub>2</sub>@TiO<sub>2</sub>@MoS<sub>2</sub> composites (15 wt% MoS<sub>2</sub>) after 3 cycles in Fig. S11 show no obvious difference between those of the fresh sample. It further demonstrates the stability of the Ti<sub>3</sub>C<sub>2</sub>@TiO<sub>2</sub>@MoS<sub>2</sub> composites. Valence band (VB) XPS spectrum of Ti<sub>3</sub>C<sub>2</sub>@TiO<sub>2</sub>@MoS<sub>2</sub> composites is measured (Fig. S12a). The VB maximum of Ti<sub>3</sub>C<sub>2</sub>@TiO<sub>2</sub>@MoS<sub>2</sub> is about 0.2 eV. Based on the above data, combined with the band gap energy (2.7 eV, Fig. S8b), the electronic band structures of Ti<sub>3</sub>C<sub>2</sub>@TiO<sub>2</sub>@MoS<sub>2</sub> composites is schematically given in Fig. S12b. It is obvious that Ti<sub>3</sub>C<sub>2</sub>@TiO<sub>2</sub>@MoS<sub>2</sub> composites is more suitable for photocatalytic hydrogen evolution as it has a more negative conduction band (CB) potential (-2.5 eV).

Photoluminescence (PL) emission spectroscopy has been used as an effective and commonly used method to reveal the transfer and separation efficiency of photogenerated charge carriers [48,49]. So that, to further comprehend the function of the photoexcited charge carriers, the photoluminescence (PL) and time-resolved fluorescence decay spectra of the samples upon 325 nm excitation are studied, as shown in Fig. 8. In general, a lower steady-state PL intensity indicates a longer lifetime and higher separation efficiency of photo-generated electron-

hole pairs, leading to higher photocatalytic activity [50]. As shown in Fig. 8a, compared with Ti<sub>3</sub>C<sub>2</sub>@TiO<sub>2</sub> composites, Ti<sub>3</sub>C<sub>2</sub>@TiO<sub>2</sub>@MoS<sub>2</sub> composites exhibit substantially depressed PL emissions, implying the photo-induced electron and holes is separated efficiently through the interface between the heterojunction of Ti<sub>3</sub>C<sub>2</sub>, TiO<sub>2</sub> and MoS<sub>2</sub>. This process can further be understood by analyzing the time-resolved fluorescence decay spectra (Fig. 8b). The intensity-average lifetimes ( $\tau$ ) of Ti<sub>3</sub>C<sub>2</sub>@TiO<sub>2</sub> composites is 0.2085 ns, which is lower than that of Ti<sub>3</sub>C<sub>2</sub>@TiO<sub>2</sub>@MoS<sub>2</sub> composites (0.2687 ns). It is believed that the increased lifetime of charge carriers in Ti<sub>3</sub>C<sub>2</sub>@TiO<sub>2</sub>@MoS<sub>2</sub> composites is associated with improved electron transport and charge-separation efficiency.

In addition to PL experiment, the photocurrent-time (I-t) and electrochemical impedance spectroscopy (EIS) were also performed to further investigate the improved carrier separation efficiency of Ti<sub>3</sub>C<sub>2</sub>@TiO<sub>2</sub>@MoS<sub>2</sub> composites. Fig. 9a shows a comparison the photocurrent-time (I-t) curves for these samples with typical on-off cycles of intermittent simulated sunlight irradiation. It can be seen that all the samples show an immediate rise in the photocurrent response when the light is on. The Ti<sub>3</sub>C<sub>2</sub>@TiO<sub>2</sub>@MoS<sub>2</sub> composites display a higher photocurrent intensity than Ti<sub>3</sub>C<sub>2</sub>@TiO<sub>2</sub> composites, which implies that the Ti<sub>3</sub>C<sub>2</sub>@TiO<sub>2</sub>@MoS<sub>2</sub> composites could achieve a higher separation and transfer efficiency of photogenerated carriers. In general, a smaller arc radius on an EIS Nyquist plot means a smaller charge-transfer resistance on the electrode surface and a higher separation efficiency of electron-hole pairs [42]. As illustrated in Fig. 9b and c, the arc size of Ti<sub>3</sub>C<sub>2</sub>@TiO<sub>2</sub>@MoS<sub>2</sub> composites is much less than Ti<sub>3</sub>C<sub>2</sub>@TiO<sub>2</sub> composites, suggesting that the Ti<sub>3</sub>C<sub>2</sub>@TiO<sub>2</sub>@MoS<sub>2</sub> composites own more effective separation of photogenerated charges. Besides, Ti<sub>3</sub>C<sub>2</sub>@TiO<sub>2</sub>@MoS<sub>2</sub> and Ti<sub>3</sub>C<sub>2</sub>@TiO<sub>2</sub> composites under solar light irradiation show decreased impedance values compared to the same samples in the dark, consistent with the increased electron conductivity of Ti<sub>3</sub>C<sub>2</sub>@TiO<sub>2</sub>@MoS<sub>2</sub> composites and Ti<sub>3</sub>C<sub>2</sub>@TiO<sub>2</sub> composites under light irradiation. Apparently, there is well agreement among PL, I-t, and EIS results, validating that Ti<sub>3</sub>C<sub>2</sub>@TiO<sub>2</sub>@MoS<sub>2</sub> composites would obviously improve the charge transfer rate, which could lead to the enhanced photocatalytic activity of Ti<sub>3</sub>C<sub>2</sub>@TiO<sub>2</sub>@MoS<sub>2</sub> composites.

On the basis of the above experimental results, a possible photocatalytic mechanism for the H<sub>2</sub> generation with Ti<sub>3</sub>C<sub>2</sub>@TiO<sub>2</sub>@MoS<sub>2</sub> composites is proposed and illustrated in Scheme 2. For Ti<sub>3</sub>C<sub>2</sub>@TiO<sub>2</sub>@MoS<sub>2</sub> composites, under light irradiation, the photoexcited electrons and holes are generated in the conduction band (CB) and valence band (VB) of TiO<sub>2</sub>, respectively. The coexposed (101) and (001) facets of TiO<sub>2</sub> can form a surface heterojunction within single TiO<sub>2</sub>. The electrons migrate from the (001) facets of TiO<sub>2</sub> to (101) facets and Ti<sub>3</sub>C<sub>2</sub> due to the excellent electron conductivity of Ti<sub>3</sub>C<sub>2</sub>. On the (101) facets of TiO<sub>2</sub>, the electrons then transport to MoS<sub>2</sub> because MoS<sub>2</sub> NSs contain several individual sandwiched S-Mo-S layers *via* weak van der Waals interactions, which lead to the abundant exposure of Mo-terminated edges with the metallic character and a high d-electron density [51].

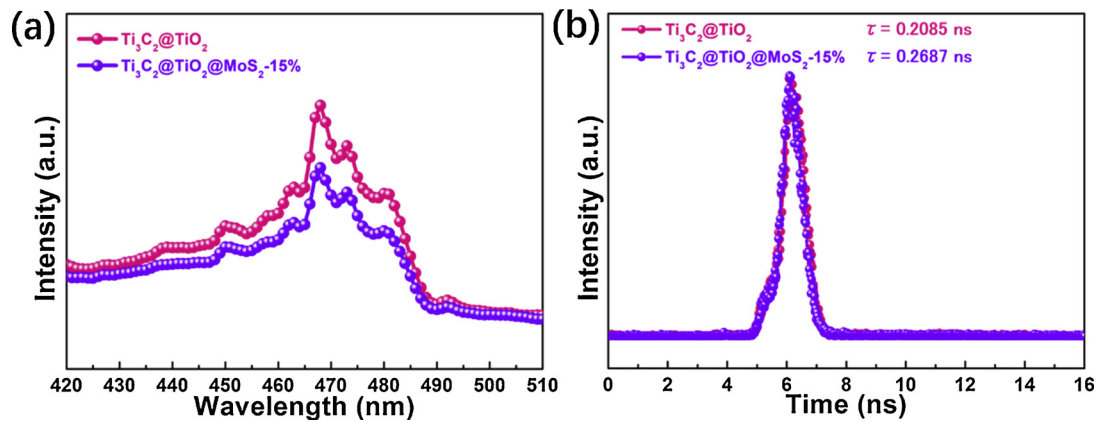


**Fig. 8.** (a) Photoluminescence (PL) and (b) time-resolved fluorescence decay spectra of  $\text{Ti}_3\text{C}_2@\text{TiO}_2$  and  $\text{Ti}_3\text{C}_2@\text{TiO}_2@15\text{ wt\% MoS}_2$ ,  $\lambda_{\text{ex}} = 325 \text{ nm}$ .

Thus, an electron-rich environment is obtained on the planar surface of  $\text{Ti}_3\text{C}_2$  and  $\text{MoS}_2$ , on which the  $\text{H}_2\text{O}$  is reduced to produce  $\text{H}_2$  [52]. The holes in (001) facets of  $\text{TiO}_2$  are consumed by the sacrificial reagents.

Although the coupling of the  $\text{Ti}_3\text{C}_2$  and  $\text{MoS}_2$  with  $\text{TiO}_2$  NSs is beneficial for photocatalytic  $\text{H}_2$  generation, we should always keep in mind that an excess of  $\text{Ti}_3\text{C}_2$  and  $\text{MoS}_2$  can cause adverse effect on the photocatalytic performance. An excess of  $\text{Ti}_3\text{C}_2$  and  $\text{MoS}_2$  lead to the light shielding effect. In detail,  $\text{Ti}_3\text{C}_2$  and  $\text{MoS}_2$  would compete with  $\text{TiO}_2$  NSs to absorb the incident photons, significantly suppressing the photoconversion efficiency of the  $\text{TiO}_2$  NSs. Thus, the control over the ratio of  $\text{TiO}_2$  NSs to  $\text{Ti}_3\text{C}_2$  and  $\text{MoS}_2$  is crucial to achieve optimized photocatalytic performance of the composite. Therefore, accurately controlled condition to regulate the formation of  $\text{Ti}_3\text{C}_2@\text{TiO}_2@15\text{ wt\% MoS}_2$  composites, incorporated with the excellent light absorption ability and enlarged specific surface area, make  $\text{Ti}_3\text{C}_2@\text{TiO}_2@15\text{ wt\% MoS}_2$  composites

superior photocatalyst for  $\text{H}_2$  evolution under light irradiation.

#### 4. Conclusions

In summary, the design concept is the *in situ* growth of  $\text{TiO}_2$  NSs on the  $\text{Ti}_3\text{C}_2$  MXene and then  $\text{MoS}_2$  NSs being introduced onto the (101) facets of  $\text{TiO}_2$  NSs with mainly exposed high-active (001) facets by combining heterojunction nanostructure construction and morphology engineering method. The obtained  $\text{Ti}_3\text{C}_2@\text{TiO}_2@15\text{ wt\% MoS}_2$  composites exhibits high photocatalytic  $\text{H}_2$  evolution activity with a rate as high as  $6425.297 \mu\text{mol h}^{-1} \text{g}^{-1}$  for the sample with 15 wt%  $\text{MoS}_2$  loading, which is higher than  $\text{Ti}_3\text{C}_2@\text{TiO}_2$  composites and  $\text{TiO}_2$  NSs. The photocatalytic reaction followed a dual-carrier-separation mechanism, where, the photogenerated electrons and holes can be respectively transferred onto (101) and (001) facets of  $\text{TiO}_2$  due to the presence of

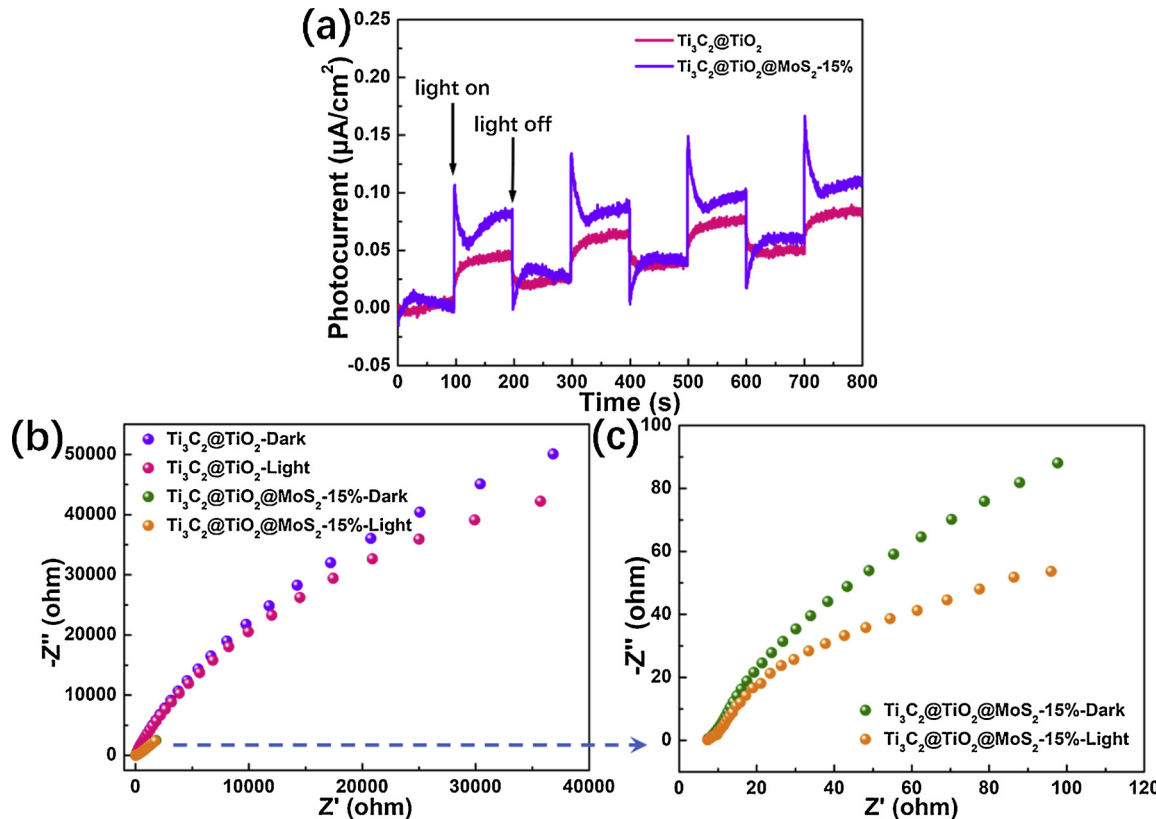
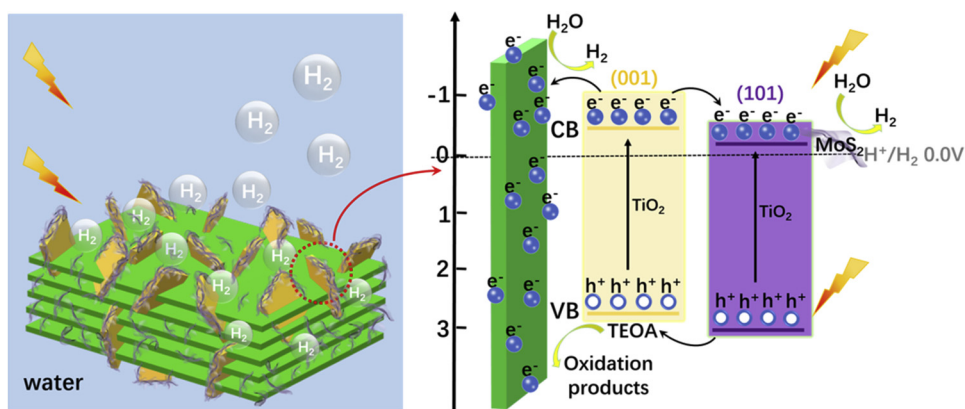


**Fig. 9.** (a) Transient photocurrent responses and (b, c) electrochemical impedance spectroscopy of  $\text{Ti}_3\text{C}_2@\text{TiO}_2$  and  $\text{Ti}_3\text{C}_2@\text{TiO}_2@15\text{ wt\% MoS}_2$  composites (15 wt%  $\text{MoS}_2$ ).



**Scheme 2.** Schematic photocatalytic reaction mechanism for  $\text{Ti}_3\text{C}_2@\text{TiO}_2@\text{MoS}_2$  composites under solar light irradiation.

surface heterojunction.  $\text{MoS}_2$  NSs on the (101) and facets of  $\text{TiO}_2$  and  $\text{Ti}_3\text{C}_2$  acted as the electron mediator and reduction cocatalyst to enhance the separation of photo-generated charges. Moreover, the close interfacial contact benefiting from *in situ* growth of  $\text{TiO}_2$  NSs on  $\text{Ti}_3\text{C}_2$  is crucial for accelerating the photogenerated electrons transfer. The large specific surface area of the unique 2D-2D-2D structure of  $\text{Ti}_3\text{C}_2@\text{TiO}_2@\text{MoS}_2$  composites and the mainly high-active exposed (001) facets governs in providing enormous surface-active sites for photocatalytic reaction. These results not only demonstrated the promise of 2D MXene based hybrids as high-performance photocatalysts, but also shed light on the loading locations and distributions of the cocatalysts in the photocatalytic hydrogen production.

## Acknowledgement

The authors are thankful for fundings from the National Natural Science Foundation of China (No.51872173), Taishan Scholarship of Young Scholars, Natural Science Foundation of Shandong Province (No. ZR2017JL020), Taishan Scholarship of Climbing Plan (No. tsdp20161006), and Key Research and Development Program of Shandong Province (No. 2018GGX102028).

## Appendix A. Supplementary data

Supplementary material related to this article can be found, in the online version, at doi:<https://doi.org/10.1016/j.apcatb.2019.01.051>.

## References

- [1] J. Huang, R. Meng, L. Zu, Z. Wang, N. Feng, Z. Yang, Y. Yu, J. Yang, *Nano Energy* 46 (2018) 20–28.
- [2] C. Meng, T. Ling, T.Y. Ma, H. Wang, Z. Hu, Y. Zhou, J. Mao, X.W. Du, M. Jaroniec, S.Z. Qiao, *Adv. Mater.* 29 (2017) 1604607.
- [3] Y. Cao, Y. Yang, Z. Ren, N. Jian, M. Gao, Y. Wu, M. Zhu, F. Pan, Y. Liu, H. Pan, *Adv. Funct. Mater.* 27 (2017) 1700342.
- [4] F. Du, H. Lu, S. Lu, J. Wang, Y. Xiao, W. Xue, S. Cao, *Int. J. Hydrogen Energy* 43 (2018) 3223–3234.
- [5] Y.J. Yuan, P. Wang, Z.J. Li, Y.Z. Wu, W.F. Bai, Y.B. Su, J. Guan, S.T. Wu, J.S. Zhong, Z.T. Yu, Z.G. Zou, *Appl. Catal. B-Environ.* 242 (2019) 1–8.
- [6] C. Li, S. Zhang, Y. Zhou, J. Li, J. Mater. Sci. Mater. El. 28 (2017) 1–8.
- [7] H. Yang, J. Tian, Y. Bo, Y. Zhou, X. Wang, H. Cui, *J. Colloids Interface Sci.* 487 (2017) 258–265.
- [8] H. Tian, K. Shen, X. Hu, L. Qiao, W.N. Zheng, *J. Alloys. Compd.* 691 (2017) 369–377.
- [9] X. Yu, X. Han, Z. Zhao, J. Zhang, W. Guo, C. Pan, A. Li, H. Liu, Z.L. Wang, *Nano Energy* 11 (2015) 19–27.
- [10] Y. Yang, H. Zhong, C. Tian, *Res. Chem. Intermediat.* 37 (2010) 91–102.
- [11] J. Yu, L. Qi, M. Jaroniec, *J. Phys. Chem. C* 114 (2010) 13118–13125.
- [12] Q. Xiang, J. Yu, *Chin. J. Catal.* 32 (2011) 525–531.
- [13] X.-Q. Gong, S. Annabella, *J. Phys. Chem. B* 109 (2005) 19560–19562.
- [14] J.C. Lei, X. Zhang, Z. Zhou, *Front. Phys.* 10 (2015) 276–286.
- [15] M. Naguib, Y. Gogotsi, *Acc. Chem. Res.* 48 (2015) 128–135.
- [16] M. Naguib, V.N. Mochalin, M.W. Barsoum, Y. Gogotsi, *Adv. Mater.* 26 (2014) 992–1005.
- [17] S. Kajiyama, L. Szabova, K. Sodeyama, H. Iinuma, R. Morita, K. Gotoh, Y. Tateyama, M. Okubo, A. Yamada, *ACS Nano* 10 (2016) 3334–3341.
- [18] X. Xie, M.Q. Zhao, B. Anasori, K. Maleski, C.E. Ren, J. Li, B.W. Byles, E. Pomerantseva, G. Wang, Y. Gogotsi, *Nano Energy* 26 (2016) 513–523.
- [19] M. Shao, Y. Shao, J.W. Chai, Y. Qu, M. Yang, Z. Wang, M. Yang, F.L. Weng, T.K. Chi, X.Q. Shi, J. Mater. Chem. A 5 (2017) 16748–16756.
- [20] M. Yu, S. Zhou, Z. Wang, J. Zhao, J. Qiu, *Nano Energy* 44 (2018) 181–190.
- [21] J. Luo, W. Zhang, H. Yuan, C. Jin, L. Zhang, H. Huang, C. Liang, X. Yang, J. Zhang, Y. Gan, *ACS Nano* 11 (2017) 2459–2469.
- [22] J. Ran, G. Gao, F.T. Li, T.Y. Ma, A. Du, S.Z. Qiao, *Nat. Commun.* 8 (2017) 13907.
- [23] X. Hu, S. Lu, J. Tian, N. Wei, X. Song, X. Wang, H. Cui, *Appl. Catal. B-Environ.* 241 (2018) 329–337.
- [24] X. Zhang, Y. Guo, J. Tian, B. Sun, Z. Liang, X. Xu, H. Cui, *Appl. Catal. B-Environ.* 232 (2018) 355–364.
- [25] C. Peng, P. Wei, X.Y. Li, Y.P. Liu, Y.H. Cao, H.J. Wang, H. Yu, F. Peng, *Nano Energy* 53 (2018) 97–107.
- [26] Y.J. Li, X.D. Deng, J. Tian, Z.Q. Liang, H.Z. Cui, *Appl. Mater. Today.* 13 (2018) 217–227.
- [27] M. Naguib, M. Kurtoglu, V. Presser, J. Lu, J. Niu, H. Min, L. Hultman, Y. Gogotsi, M.W. Barsoum, *Adv. Mater.* 23 (2011) 4207–4207.
- [28] C. Yang, Y. Liu, X. Sun, Y. Zhang, L. Hou, Q. Zhang, C. Yuan, *Electrochim. Acta* 271 (2018) 165–172.
- [29] X. Liu, Z. Chang, L. Luo, T. Xu, X. Lei, J. Liu, X. Sun, *Cheminform* 45 (2014) 1889–1895.
- [30] Z. Wang, Z.X. Low, X. Zeng, B. Su, Y. Yin, C. Sun, T. Williams, H. Wang, X. Zhang, *Int. J. Hydrogen Energy* 43 (2017) 1508–1515.
- [31] Y. Dong, Z.S. Wu, S. Zheng, X. Wang, J. Qin, S. Wang, X. Shi, X. Bao, *ACS Nano* 11 (2017) 4792–4800.
- [32] W. Zhou, Z. Yin, Y. Du, X. Huang, Z. Zeng, Z. Fan, H. Liu, J. Wang, H. Zhang, *Small* 9 (2013) 140–147.
- [33] Y.J. Yuan, Z.J. Li, S.T. Wu, D.Q. Chen, L.X. Yang, D.P. Cao, W.G. Tu, Z.T. Yu, Z.G. Zou, *Chem. Eng. J.* 350 (2018) 335–343.
- [34] B. Chen, E. Liu, F. He, C. Shi, C. He, J. Li, N. Zhao, *Nano Energy* 26 (2016) 541–549.
- [35] L. Zheng, S. Han, H. Liu, P. Yu, X. Fang, *Small* 12 (2016) 1527–1536.
- [36] C. Liu, L. Wang, Y. Tang, S. Luo, Y. Liu, S. Zhang, Y. Zeng, Y. Xu, *Appl. Catal. B-Environ.* 164 (2015) 1–9.
- [37] S.L. Harmer, L.V. Goncharova, R. Kolarova, W.N. Lennard, M.A. Muñozmárquez, I.V. Mitchell, H.W. Nesbitt, *Surf. Sci.* 601 (2007) 352–361.
- [38] K.S.W. Sing, *Pure Appl. Chem.* 57 (1985) 603–619.
- [39] R. Wang, S. Wang, Y. Zhang, D. Jin, X. Tao, L. Zhang, J. Mater. Chem. A 6 (2018) 1017–1027.
- [40] J. Zhang, L. Qian, F. Wei, J. Xi, Z. Ji, F. Alkaline, J. Xi, Z. Ji, J. Am. Ceram. Soc. 97 (2014) 2615–2622.
- [41] L.W. Yu, F. Xu, B. Xue, Z. Luo, Q. Zhang, B. Bao, S. Su, L. Weng, W. Huang, L. Wang, *Nanoscale* 6 (2014) 5762–5769.
- [42] Z. Liang, X. Bai, P. Hao, Y. Guo, Y. Xue, J. Tian, H. Cui, *Appl. Catal. B-Environ.* 243 (2019) 711–720.
- [43] X. Hu, Y. Li, J. Tian, H. Yang, H. Cui, J. Ind. Eng. Chem. 45 (2016) 189–196.
- [44] Y. Liu, H. Du, X. Zhang, Y. Yang, M. Gao, H. Pan, *Chem. Commun.* 52 (2015) 705–708.
- [45] H. Ghassemi, W. Harlow, O. Mashtalir, M. Beidaghi, M.R. Lukatskaya, Y. Gogotsi, M.L. Taheri, J. Mater. Chem. A 2 (2014) 14339–14343.
- [46] J. Wang, P. Rao, W. An, J. Xu, Y. Men, *Appl. Catal. B-Environ.* 195 (2016) 141–148.
- [47] M. Mazurais, C. Lescot, P. Retailleau, P. Dauban, *Appl. Catal. B-Environ.* 1 (2014) 66–79.
- [48] H. Li, Y. Liu, Y. Cui, W. Zhang, C. Fu, X. Wang, *Appl. Catal. B-Environ.* 183 (2016) 426–432.
- [49] Y.J. Yuan, Y. Yang, Z.J. Li, D.Q. Chen, S.T. Wu, G.L. Fang, W.F. Bai, M.Y. Ding, L.X. Yang, D.P. Cao, Z.T. Yu, Z.G. Zou, *ACS Appl. Energy Mater.* 1 (2018) 1400–1407.
- [50] M. Schwartzman, V. Sidorov, D. Ritter, Y. Paz, *Semicond. Sci. Tech.* 16 (2001) L68–L71.
- [51] S. Guo, X. Li, J. Zhu, T. Tong, B. Wei, *Small* 12 (41) (2016) 5649–5649.
- [52] J. Liu, Y. Liu, D. Xu, Y. Zhu, W. Peng, Y. Li, F. Zhang, X. Fan, *Appl. Catal. B-Environ.* 241 (2019) 89–94.